Fiber Formation Mechanisms of Jet-Assisted Wet Spinning (JAWS)

Zehao Pan,[1] Barath Venkateswaran,[2] Janine K. Nunes,[1] Pierre-Thomas Brun,[2] and Howard A. Stone[1]
[1]*Department of Mechanical and Aerospace Engineering, Princeton University, Princeton, NJ 08544, USA*
[2]*Department of Chemical and Biological Engineering, Princeton University, Princeton, NJ 08544, USA*
(*hastone@princeton.edu)
(Dated: November 18, 2024)

In fiber spinning of photopolymers, surface tension limits the diameter of the fiber that can be produced due to the Rayleigh-Plateau instability. Submerging a pre-fiber jet in a miscible environment liberates the system from capillary effects, thus allowing the jet to be stretched into thin threads without instability. In this work, we systematically investigated a spinning method using miscible liquids, called jet-assisted wet spinning (JAWS), where stretching is achieved by a nearby submerged liquid jet. The diameter of the pre-fiber jet is a function of its flow rate and position relative to the assisting submerged liquid jet. A particular case where the main jet is modeled as the Landau-Squire jet is used to demonstrate the tracer-like thinning behavior of the pre-fiber jet. Experiments show that buoyancy has a significant impact on the pre-fiber jet diameter because of its influence on the entrainment trajectory. Overall, our results demonstrate the potential for parallelization of JAWS for high-throughput fiber production.

Fiber spinning through photopolymerization has been widely applied to make fibers in biomedical applications [1–4], material sciences [5], and the physical sciences [6, 7]. For example, blow spinning and electrospinning have been used to spin photopolymeric fibers in the production of non-wovens or in-situ applications [8–10]. In general, polymer spinning methods (melt spinning, solution spinning, blow spinning, and electrospinning) are limited to solutions or melts with spinnable rheological properties, such that surface-tension-driven instabilities are suppressed [11–13]. In addition, microfluidic-based spinning has been applied to many photopolymerizable materials with exceptional control over the fiber dimensions and uniformity [14–19], but performing a polymerization reaction in a microfluidic channel poses a risk of irreversible clogging of the channel [20, 21].

Here, we introduce an unbounded flow methodology designed to circumvent the aforementioned challenge in microfluidics. Jet-Assisted Wet Spinning (JAWS) relies on the flow field produced by a high-speed submerged liquid jet to stretch a nearby slower-flowing,photopolymerizable, and miscible pre-fiber jet such that its diameter decreases significantly. After stretching, the pre-fiber jet is then solidified using light-induced free radical polymerization (Figure 1(a)). Because solidification occurs in a liquid bath instead of inside a microchannel, clogging is avoided. In addition, we demonstrate the potential for parallel spinning multiple fibers using JAWS for high-throughput applications.

JAWS has been applied to make entangled fibers [22], yet the physics that governs fiber formation remains to be understood. Specifically, the momentum of the assisting jet and the location, viscosity, buoyancy, and momentum of the pre-fiber jet could all play roles in determining the diameter variation of the pre-fiber jet and thus the diameter of the final polymerized fiber. In this paper, we use experiments and a minimal tracer model to investigate systematically the influence of the aforementioned parameters on the pre-fiber jet diameter.

The experimental setup for JAWS is shown in Figure 1(a). The pre-fiber solution for a PEGDA (polyethylene glycol diacrylate) hydrogel (Sigma) was injected at a constant flow rate Q_2 near a fast-moving liquid jet with a constant flow rate Q_1 while both jets were submerged in a miscible liquid bath in an acrylic box. The solution contains 50 vol % PEGDA, 1 vol % 2-hydroxy-2-methylpropiophenone (photoinitiator), and 49 vol % deionized water. During a typical experiment cycle, around 1 mL of pre-fiber solution is lost to the liquid bath of around 1 L. This comes to around 0.001 vol % of photoinitiator contamination; hence, we can neglect its effect on fiber production. Depending on the experiment, the bath can be pure water or a sodium chloride solution, but the liquid used for the assisting jet and the bath are always identical. The liquid bath and the assisting jet have density ρ_1, while the pre-fiber jet has density ρ_2. The blunt needles for dispensing water and pre-fiber solutions are placed in parallel at depths H_1 and H_2 below the water-air interface and the two needles are separated by distance L. The blunt needle for the pre-fiber jet may be bent to provide enough clearance, forming "⊣" shape with the needle for the assisting jet when the two needles are placed next to each other. The inner radii of the needles are R_1 and R_2 for the assisting jet and the pre-fiber jet, respectively. Both H_1 and H_2 are at least 100 times larger than R_1, which reduces the influence of the bath-air boundary on the flow field. The light-based polymerization system is the same as previous studies [23]. To image the flow field generated by the assisting jet, polystyrene particles were added to the bath. The particles were illuminated by a laser light sheet and tracked using a high-speed camera.

As an illustration of the stretching of a pre-fiber jet by an assisting jet, we show in Figure 1(b) two samples of fibers made with or without an assisting jet in typical operating conditions. Using the same flow rate of the pre-fiber solution, the diameter of the fibers made with the assisting jet is five times smaller than the fibers made without the assisting jet.

To control the fiber diameter produced by JAWS, it is essential to control the pre-fiber jet diameter by adjusting the flow rates and the nozzle positions. We show the effect of varying the positions of the pre-fiber jet under neutral buoyancy conditions ($\rho_1 = \rho_2$) in Figure 1(c). In configurations B and C, the pre-fiber jet nozzle was placed further from the assisting jet nozzle. In terms of H_2, A > B > C ; in terms of L, A < B = C. Tracing the centerlines of the pre-fiber jets, their radii R_{pf}

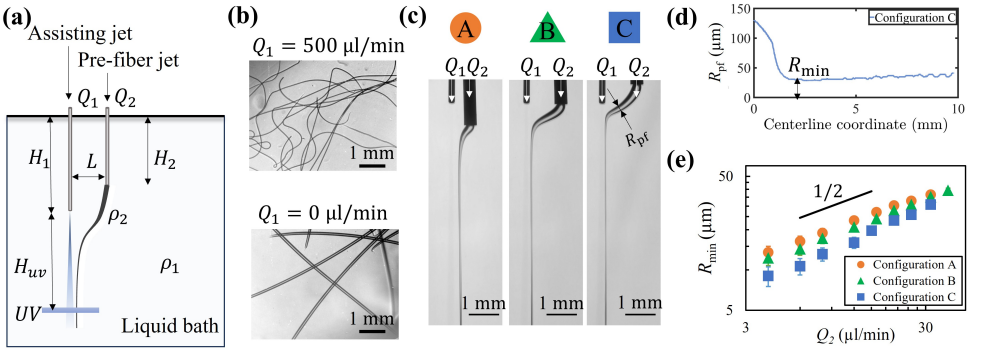

FIG. 1. (a) Schematic illustration of the Jet-Assisted Wet Spinning (JAWS) setup used in this work. A high-speed jet (flow rate Q_1) is issued into a bath of the same liquid with density ρ_1, which stretches an adjacent pre-fiber jet (flow rate Q_2) with density ρ_2. The photo-reactive pre-fiber jet can be solidified upon exposure to UV light at position H_{uv} downstream of the assisting jet nozzle. The inner radii of the nozzles for the assisting jet and the pre-fiber jet are $R_1 = 40\ \mu$m and $R_2 = 150\ \mu$m, respectively. (b) PEGDA fibers are made with or without the assisting jet, while other conditions are the same. $Q_1 = 500\,\mu\text{l}\cdot\text{min}^{-1}$ ($\text{Re}_1 = 60$) and $Q_2 = 5\,\mu\text{l}\cdot\text{min}^{-1}$ ($\text{Re}_2 = 0.16$) for both cases. (c) Snapshots of experimental images of JAWS for configurations A, B, and C. Dye is added to the assisting jet and the pre-fiber jet for visualization. The flow rates of the pre-fiber jet and the assisting jet are 20 $\mu\text{l}\cdot\text{min}^{-1}$ and 540 $\mu\text{l}\cdot\text{min}^{-1}$ respectively. Sodium chloride was added to the bath and the high-speed jet solution so that $\rho_1 = \rho_2 = 1.06\times10^3\ \text{kg}\cdot\text{m}^{-3}$. (d) The pre-fiber jet radii R_{pf} of configuration C along its centerline. The minimum radius, R_{min}, along a pre-fiber jet profile is indicated. (e) The R_{min} plotted against Q_2 for configurations A, B, and C while other parameters are kept the same. The error bars represent the standard deviation of three independent measurements.

can be quantified. As an example, we show in Figure 1(d) the R_{pf} profile of configuration C. In all cases, the pre-fiber jets have minimum radii R_{min} over a region of about 1 mm along the centerline. R_{min} limits how much the pre-fiber jet can be thinned by JAWS, and is thus crucial to the method.

We measured R_{min} of the pre-fiber jets for configurations A, B, and C and for various Q_2, as displayed in Figure 1(e). We observed that among the three configurations, configuration A produces the largest R_{min} among all three configurations despite configuration A having the closest separation between the two nozzles. The measured R_{min} closely follows the $R_{min} \propto Q_2^{1/2}$ scaling, as suggested by mass conservation of the pre-fiber jet.

To understand the conditions that govern R_{min} in Figure 1(e), we used particle tracers to characterize the streamlines surrounding the assisting jet in the absence of the pre-fiber jet. Each particle is represented by a symbol and its location at each time frame is displayed in Figure 2(a).

The streamlines follow the self-similar solutions of the Landau-Squire (LS) jet [24, 25], an exact self-similar solution (in spherical coordinates) of the Navier-Stokes equations for a point source of momentum (Supplementary Material). When the jet is issued from a nozzle, the origin of the LS jet is located at a distance r^* inside the nozzle, where

$$\frac{r^*}{R_1} = 0.2\text{Re}_1 \tag{1}$$

and $\text{Re}_1 \equiv Q_1/(\pi R_1 \nu)$ is the Reynolds number of the assisting jet (ν is the kinematic viscosity of the jet). The expression for r^* is derived based on momentum matching with the Schlichting jet [26, 27], which is a degenerate form of the Landau-Squire jet at moderate to high Reynolds numbers. Note that a simplified form of the LS jet has already been used to describe the flow field of a submerged jet in the low-Reynolds-number limit [28, 29]. In JAWS, Re_1 is typically larger than 30, so the use of the full solution of the LS jet is necessary.

Experimentally measured streamlines and derived streamlines from the LS jet show good agreement. The streamlines from the LS jet has the form $rf(\theta) = c$ (Equation (S4) in Supplementary Material), where c is a constant along a streamline. Thus, we rescale both experimental and theoretical streamlines by the distances to the origin, r_n, at an angle $\theta = \pi/4$, i.e., $r_n f(\pi/4) = c_n$. Following the rescaling, all theoretical streamlines collapse onto the same curve due to the self-similarity, which is shown as the solid curve in Figure 2(b). The experimentally measured streamlines collapse near this curve, especially for those that have a larger r_n. The deviation of streamlines with smaller r_n is expected (e.g., streamlines labeled with circles and diamonds in Figure 2(b)), because the LS jet solution is an idealized point source of momentum that does not account for the presence of a nozzle.

In JAWS, a pre-fiber stream is placed in the flow field created by the LS jet. Many factors could affect its speed and trajectory: the pre-fiber jet is frequently ten times more viscous than the bath liquid so that the stretching of the pre-fiber jet could be suppressed due to the viscous stresses for bending and thinning [30, 31]. The momentum of the pre-fiber jet, although small compared to the assisting jet, may be much higher than the momentum of the local flow field where the pre-fiber nozzle is placed. Because of the miscibility of the

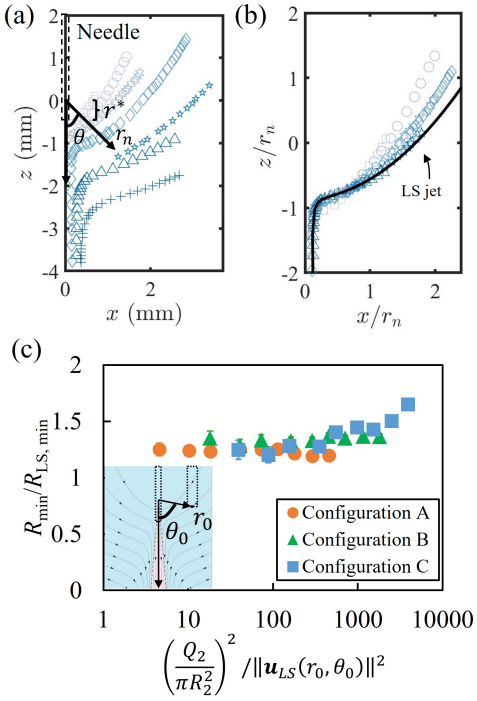

FIG. 2. **Comparison between $R_{\min}$ and $R_{\mathrm{LS,min}}$.** (a) Particle traces near the assisting jet. Each symbol represents a tracer particle. The origin of the spherical coordinate system was placed a distance r^* inside the nozzle according to Equation (1). r_n is defined as the distance from the origin to a streamline at $\theta = 45°$. $\mathrm{Re}_1 = 60$. (b) Collapsed streamlines by normalizing the coordinates of each streamline with its r_n. The prediction from the LS jet solution is displayed as the solid line. $\mathrm{Re}_1 = 60$ for both the experiment and the LS jet. (c) Collapsed $R_{\min}$ using the $R_{\mathrm{LS,min}}$ of a tracer jet. The horizontal axis is the ratio of the momentum fluxes of the pre-fiber jet and the LS jet at the pre-fiber nozzle. Inset shows the (r_0, θ_0) of configuration C in the LS jet flow field generated by the assisting jet. The dotted squares in the inset represent the nozzles.

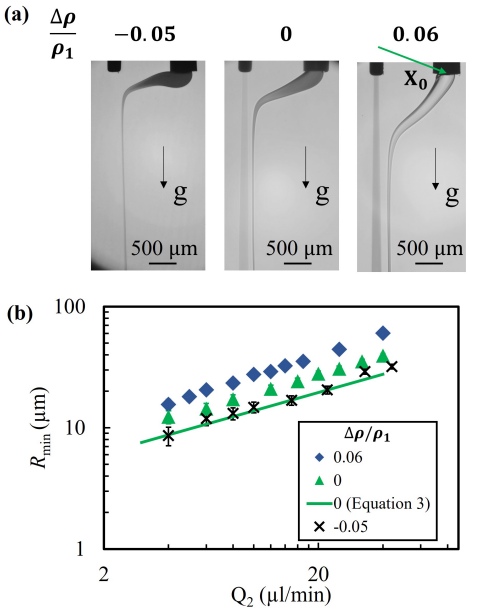

FIG. 3. **The effect of buoyancy on $R_{\min}$ in configuration B.** (a) Snapshots of JAWS operating with different $\Delta\rho/\rho_1$. $\mathrm{Re}_1 = 60$ and the flow rate of the pre-fiber jet is 6 $\mu\mathrm{l}\cdot\mathrm{min}^{-1}$. The effect of buoyancy can be seen from the trajectory of the pre-fiber jet: a denser bath leads to an upward bending trajectory, while, in contrast, a less dense bath leads to a downward bending trajectory. The arrow in the last panel indicates $\mathbf{X}_0$. (b) $R_{\min}$ measured at different Q_2 for three cases of $\Delta\rho > 0, = 0$ and < 0. The data points represent experimental measurements. The line represents $R_{\mathrm{LS,min}}$ calculated from Equation (3). The error bars represent the standard deviation of three independent measurements.

pre-fiber jet, diffusion could affect the diameter of the pre-fiber jet when the jet is very thin.

When comparing the trajectories of the pre-fiber jets and the streamlines of the LS solution, they are found to overlap in most cases. Thus, here we compare the experimentally measured $R_{\min}$ with a scenario where the pre-fiber jet simply traces the steady flow field described by the LS solution. The calculated $R_{\mathrm{LS,min}}$ can be derived using volume conservation as the pre-fiber jet reaches the maximum speed $u_{\max}$ according to the LS solution:

$$R_{\mathrm{LS,min}} \equiv \sqrt{\frac{Q_2}{\pi u_{\max}}}. \tag{2}$$

Now we derive the expression of $u_{\max}$ using the tracer assumption. Following the coordinate matching between the LS jet and the nozzle for the assisting jet flow from Equation (1), the coordinate of the nozzle for the pre-fiber jet can be defined in the spherical coordinate system of the LS jet as $\mathbf{X}_0 = (r_0, \theta_0)$, where $r_0 = \sqrt{(H_1 - r^* - H_2)^2 + L^2}$ and $\cos\theta_0 = (H_2 + r^* - H_1)/r_0$. Due to axisymmetry, any streamline in the LS jet that passes $\mathbf{X}_0$ is on a tube-shaped stream surface. All the stream surfaces in the LS flow have a minimum radius, called the 'throat' of the jet, where the speed of a tracer particle on the stream surface is the highest. If we define the $u_{\max}$ in Equation (2) as the magnitude of velocity at the throat of a stream surface passing $\mathbf{X}_0$, the theoretical minimum for $R_{\min}$ based on the LS solution is (see the Supplementary Material):

$$R_{\mathrm{LS,min}} = \sqrt{\left(8/\mathrm{Re}_1^2 + 1\right)^2 - 1}\sqrt{\frac{cQ_2}{4\pi\nu^2}}, \tag{3}$$

where c is the stream function constant that depends on the

placement of the pre-fiber nozzle at $\mathbf{X}_0$:

$$c = \frac{2\nu r_0\left(1-\cos^2\theta_0\right)}{8/\mathrm{Re}_1^2+1-\cos\theta_0}. \tag{4}$$

The jet diameter can be tuned by adjusting the position of the pre-fiber nozzle or adjusting the flow rates. We compare the measured $R_{\min}$ reported in Figure 1(e) with $R_{\mathrm{LS,min}}$, as shown in Figure 2(c). The ratio $R_{\min}/R_{\mathrm{LS,min}}$ is plotted against the ratio of the momentum fluxes of the pre-fiber jet $\rho_2\left(Q_2/(\pi R_2^2)\right)^2$ and the LS jet $\rho_1 \boldsymbol{u}_{\mathrm{LS}}^2(\mathbf{X}_0)$ at the pre-fiber nozzle, where $\boldsymbol{u}_{\mathrm{LS}}(\mathbf{X}_0)$ is the velocity of the LS jet solution at $\mathbf{X}_0$. Over two decades of the momentum ratio, $R_{\min}/R_{\mathrm{LS,min}}$ falls in a range between 1.2 - 1.5 for configuration A and B, however, the relationship breaks down for configuration C at high momentum flux ratios. The observation that $R_{\min}/R_{\mathrm{LS,min}} > 1$ is also not surprising because the viscous stresses that drive the thinning of the pre-fiber jet are reduced as the pre-fiber jet approaches the speed of the surrounding fluid [32].

In JAWS, the pre-fiber jet often has a different density than the bath liquid. For example, when using a PEGDA solution as the pre-fiber solution and water as the bath liquid, the density difference $\Delta\rho/\rho_1 = (\rho_2-\rho_1)/\rho_1$ could range from 0 - 12% depending on the concentration of the PEGDA solution. Due to the coupled relationship between the density and the viscosity of the PEGDA solution, the effect of density on the pre-fiber jet could be mistaken as a viscous effect.

We experimentally investigated the effect of density of the pre-fiber jet using configuration B, as shown in Figure 3. We added sodium chloride to the bath liquid to change its density while using the same pre-fiber solution. The density of the bath varies between 0.95 to 1.06 $\mathrm{kg\cdot m^{-3}}$, while the kinematic viscosity of the bath varies between 0.89 to 1.09 $\mathrm{mm^2\cdot s^{-1}}$. Different Q_1 values are used to ensure $\mathrm{Re}_1 = 60$ when using a bath with a different kinematic viscosity. The snapshots of the pre-fiber jets are shown in Figure 3(a). Compared to the pre-fiber solution with $\Delta\rho = 0$, the pre-fiber jet moves in the direction of gravity when $\Delta\rho > 0$, whereas the pre-fiber jet is displaced in the opposite direction of gravity when $\Delta\rho < 0$.

Similar to the pre-fiber jet profile in Figure 1(d), the radius of the pre-fiber jet has a minimum value, $R_{\min}$, along its centerline. In order to quantify the effect of buoyancy on $R_{\min}$, we plot $R_{\min}$ versus Q_2 in Figure 3(b). Compared to the neutrally buoyant scenario, the pre-fiber jet that is 6 % more dense than the bath has a 30% increase in $R_{\min}$; the pre-fiber jet that is 5 % less dense than the bath has a 25 % decrease in $R_{\min}$.

We can understand the effect of buoyancy on the $R_{\min}$ with scaling arguments. The buoyancy force per unit length on a pre-fiber jet scales as $\Delta\rho g\pi R_{pf}^2$. According to slender body theory [33, 34], the hydrodynamic drag force per unit length at leading order scales as $\mu\boldsymbol{u}_g$, where $\boldsymbol{u}_g$ is the velocity of the pre-fiber jet relative to the local LS jet solution. Balancing the buoyancy and hydrodynamic drag forces, $\boldsymbol{u}_g$ scales as $\Delta\rho g\pi R_{pf}^2/\mu$, where μ is the dynamic viscosity of the bath. Buoyancy affects the pre-fiber jet for a time of the order $L/\boldsymbol{u}_{\mathrm{LS}}(\mathbf{X}_0)$, during which the stream function constant in Equation (4) changed from c to c^g, where c^g/c is of the order $\left(r_0+\boldsymbol{u}_g L/\boldsymbol{u}_{\mathrm{LS}}(\mathbf{X}_0)\right)/r_0$. Using the relationship in Equation (3), the ratio between the new $R_{\mathrm{LS,min}}^g$ and the buoyancy-free $R_{\mathrm{LS,min}}$ scales as $\sqrt{c^g/c}$, i.e.,

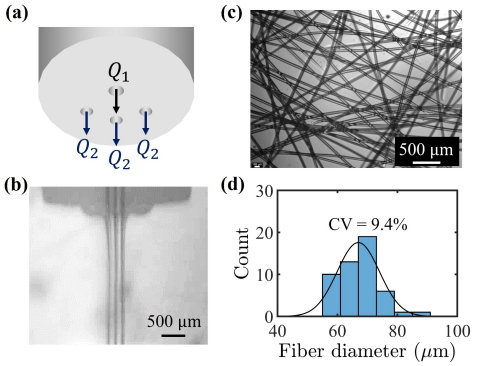

FIG. 4. **Multiple pre-fiber jets in a single JAWS system.** (a) The nozzles for the parallel JAWS configuration, where the assisting nozzle radius is $R_1 = 150$ μm and pre-fiber nozzle radius is $R_2 = 125$ μm. The pre-fiber nozzles are 0.8 mm away from the assisting nozzle. (b) Experimental snapshots showing three pre-fiber jets being stretched by the assisting jet. $\mathrm{Re}_1 = 19.2$ and $Q_2 = 10$ $\mu\mathrm{l\cdot min^{-1}}$. (c) PEGDA fibers produced using the three-jet JAWS system. (d) The diameter distribution of 50 fibers produced by the three-jet JAWS system.

$$\frac{R_{\mathrm{LS,min}}^g}{R_{\mathrm{LS,min}}} \propto \sqrt{\frac{\left(r_0+\boldsymbol{u}_g L/\boldsymbol{u}_{\mathrm{LS}}(\mathbf{X}_0)\right)}{r_0}}. \tag{5}$$

Equation (5) quantifies the effect of buoyancy in leading order. Setting $R_{pf} = R_{\mathrm{LS,min}}$ for $\boldsymbol{u}_g$, we found $R_{\mathrm{LS,min}}^g$ is no more than 20 % higher or lower than $R_{\mathrm{LS,min}}$ for cases of $\Delta\rho > 0$ and < 0, in reasonable agreement with experimental data.

An attractive aspect of JAWS is leveraging the axisymmetry of the assisting jet to spin multiple fibers in parallel. The highest number of pre-fiber jets possible depends on the pre-fiber jet diameter and its distance to the assisting jet. For demonstration, we used 3D printing to create a JAWS system with three pre-fiber jets surrounding one assisting jet, as shown in Figure 4(a). Each pre-fiber jet has flow rate Q_2 while the assisting jet flow rate is still Q_1. The distance between the holes (nozzles) that issue pre-fiber jets and the assisting jet are the same so that the conditions for the entrainment of the pre-fiber jets are the same. Therefore, the same fibers can be made with three times the throughput. An experimental snapshot of the three pre-fiber jet JAWS system in operation is shown in Figure 4(b). The pre-fiber jet can be seen being focused and stretched by the assisting jet. The fibers produced through this setup are shown in Figure 4(c) where the diameter of the fiber $d_f = 67 \pm 6$ μm. The distribution of d_f have a coefficient of variation (CV) of 9.4%, as shown in Figure 4(d).

The JAWS system can be readily adopted to making other types of materials. For example, stereolithography resin is a

photopolymer that dissolves in isopropyl alcohol (IPA). We have used commercial stereolithography resin formulation as the pre-fiber jet and IPA as the bath and assisting jet to make stretchable fibers (data not shown), even when the pre-fiber jet is 5000 times more viscous than the bath liquid.

SUPPLEMENTARY MATERIAL

Derivation for $R_{\mathrm{LS,min}}$ using the Landau-Squire solution can be found in the Supplementary Material.

ACKNOWLEDGMENTS

This work is supported by NSF Grant No. CMMI-1661672 and the Hong Kong RGC Research Impact Fund No. R7072-18. This research is partially supported by NSF through the Princeton University (PCCM) Materials Research Science and Engineering Center DMR-2011750.

DATA AVAILABILITY STATEMENT

The data that support the findings of this study are available within the article and its supplementary material.

CONFLICT OF INTEREST STATEMENT

Z.P., J.K.N, and H.A.S have U.S. Patent Application No. 18/771,469 pending.

AUTHOR CONTRIBUTIONS

Z.P., J.K.N. and H.A.S. conceptualized the research; Z.P. and B.V. conducted the investigation; Z.P. wrote the original draft; all authors contributed to review and editing.

[1] J. Nunes, S. Tsai, J. Wan, and H. A. Stone, Journal of Physics D: Applied Physics **46**, 114002 (2013).
[2] X. Du, Q. Li, G. Wu, and S. Chen, Advanced Materials **31**, 1903733 (2019).
[3] C. B. Highley, K. H. Song, A. C. Daly, and J. A. Burdick, Advanced Science **6**, 1801076 (2019).
[4] W. Razzaq, C. A. Serra, C. Dussouillez, N. Kharouf, I. A. A. Mejía, A. Kichler, and D. Chan-Seng, RSC Applied Polymers **2**, 62 (2024).
[5] K. Shanmuganathan, R. K. Sankhagowit, P. Iyer, and C. J. Ellison, Chemistry of Materials **23**, 4726 (2011).
[6] E. A. Kolchanova, N. Kolchanov, and A. S. Sidorov, Interfacial Phenomena and Heat Transfer **11**, 65 (2023).
[7] C. Duprat, Annual Review of Fluid Mechanics **54**, 443 (2022).
[8] C. J. Ellison, A. Phatak, D. W. Giles, C. W. Macosko, and F. S. Bates, Polymer **48**, 3306 (2007).
[9] S.-S. Kim, H. Ha, and C. J. Ellison, ACS Sustainable Chemistry & Engineering **6**, 8364 (2018).
[10] A. Banerji, K. Jin, K. Liu, M. K. Mahanthappa, and C. J. Ellison, Macromolecules **52**, 6662 (2019).
[11] R. Larson, Journal of Non-Newtonian Fluid Mechanics **12**, 303 (1983).
[12] L. Palangetic, N. K. Reddy, S. Srinivasan, R. E. Cohen, G. H. McKinley, and C. Clasen, Polymer **55**, 4920 (2014).
[13] A. Y. Malkin, A. Semakov, I. Y. Skvortsov, P. Zatonskikh, V. Kulichikhin, A. Subbotin, and A. Semenov, Macromolecules **50**, 8231 (2017).
[14] W. Jeong, J. Kim, S. Kim, S. Lee, G. Mensing, and D. J. Beebe, Lab on a Chip **4**, 576 (2004).
[15] J. K. Nunes, K. Sadlej, J. I. Tam, and H. A. Stone, Lab on a Chip **12**, 2301 (2012).
[16] M. A. Daniele, K. Radom, F. S. Ligler, and A. A. Adams, RSC Advances **4**, 23440 (2014).
[17] X. Shi, S. Ostrovidov, Y. Zhao, X. Liang, M. Kasuya, K. Kurihara, K. Nakajima, H. Bae, H. Wu, and A. Khademhosseini, Advanced Functional Materials **25**, 2250 (2015).
[18] W. Lan, Y. Du, X. Guo, A. Liu, S. Jing, and S. Li, Industrial & Engineering Chemistry Research **57**, 212 (2018).
[19] M. Hu, R. Deng, K. M. Schumacher, M. Kurisawa, H. Ye, K. Purnamawati, and J. Y. Ying, Biomaterials **31**, 863 (2010).
[20] Z. Chen, Z. Lv, Z. Zhang, D. A. Weitz, H. Zhang, Y. Zhang, and W. Cui, in *Exploration*, Vol. 1 (Wiley Online Library, 2021) p. 20210036.
[21] D. Boskovic and S. Loebbecke, Nanotechnology Reviews **3**, 27 (2014).
[22] Z. Pan, J. K. Nunes, C. Duprat, H. C. Shum, and H. A. Stone, Nature Communications **14**, 1242 (2023).
[23] M. Slutzky, H. A. Stone, and J. K. Nunes, Soft Matter **15**, 9553 (2019).
[24] L. D. Landau and E. M. Lifshitz, *Fluid Mechanics* (Elsevier, 2013).
[25] H. B. Squire, The Quarterly Journal of Mechanics and Applied Mathematics **4**, 321 (1951).
[26] E. N. da C Andrade and L. C. Tsien, Proceedings of the Physical Society **49**, 381 (1937).
[27] G. Krishnan and K. Mohseni, AIAA Journal **47**, 2273 (2009).
[28] N. Laohakunakorn, B. Gollnick, F. Moreno-Herrero, D. G. Aarts, R. P. Dullens, S. Ghosal, and U. F. Keyser, Nano Letters **13**, 5141 (2013).
[29] E. Secchi, S. Marbach, A. Niguès, A. Siria, and L. Bocquet, Journal of Fluid Mechanics **826**, R3 (2017).
[30] P.-T. Brun, N. M. Ribe, and B. Audoly, Physics of Fluids **24**, 043102 (2012).
[31] J. Teichman and L. Mahadevan, Journal of Fluid Mechanics **478**, 71 (2003).
[32] S. Sinha-Ray, S. Sinha-Ray, A. L. Yarin, and B. Pourdeyhimi, Polymer **56**, 452 (2015).
[33] R. G. Cox, Journal of Fluid Mechanics **44**, 791 (1970).
[34] B. Marchetti, V. Raspa, A. Lindner, O. Du Roure, L. Bergougnoux, É. Guazzelli, and C. Duprat, Physical Review Fluids **3**, 104102 (2018).